Oscillation Suppression Considering Characteristics of Interaction Energy in Grid-connected DFIG-based Wind Farms via VSC-HVDC Transmission System

Jing Ma, *Senior Member*, *IEEE*, Ningsai Su, Yawen Deng, Weifeng Xia, Honglu Xu, and Yaqi Shen

***Abstract*—For doubly-fed induction generator (DFIG) -based wind farms connected to flexible DC transmission system, the oscillation suppression after fault clearance proves very difficult. Addressing this problem, this paper constructs the dynamic energy model of the interconnected system, reveals the mechanism of oscillation instability after fault clearance, and designs an oscillation suppression strategy. First, by considering the dynamic characteristics of the control links in grid-connected DFIG-based wind farms via voltage source converter based high-voltage direct current (VSC-HVDC) transmission system, the interconnected system is divided into several subsystems, and the energy model of each subsystem is constructed. Furthermore, the magnitudes and directions of different interaction energy items are quantitatively analyzed, so that the key control links that transmit and magnify the system energy can be identified. On this basis, the corresponding supplementary control links are designed to suppress the system oscillation. Finally, the accuracy and effectiveness of the proposed oscillation suppression strategy are verified by hardware-in-loop tests. The results prove that the *d*-axis subsystem of DFIG grid-side converter (GSC) current inner loop, phase-locked loop (PLL), and *q*-axis subsystem of VSC-HVDC voltage outer loop are the key links that induce the oscillation to occur, and the proposed strategy shows promising results in oscillation suppression.**

***Index Terms*—Doubly-fed induction generator (DFIG), voltage source converter (VSC), flexible DC power transmission, stability analysis, oscillation suppression.**

I. Introduction

In recent years, voltage source converter based high-voltage direct current (VSC-HVDC) transmission has gradually become one of the mainstream ways to transmit the wind power generated by doubly-fed induction generators (DFIGs) [1]. After a fault is cleared, the complex interaction between DFIG and VSC-HVDC may cause the oscillation, thus intimidating the stable operation of power system. Therefore, it is very important to study the mechanism of oscillation in grid-connected DFIG-based wind farms via VSC-HVDC transmission system after fault clearance, and propose effective oscillation suppression strategies.

Currently, small-signal oscillation stability analysis for grid-connected DFIG-based wind farms via VSC-HVDC transmission system can be mainly achieved from the modal analysis method and the impedance analysis method. The small-signal modeling method for grid-connected wind farm via VSC-HVDC transmission system has been detailed in [2]. And based on the small-signal model of the system, the oscillation stability of the grid-connected DFIG-based wind farms has been analyzed by the modal analysis method in [3], and the influences of LCL filter, parameters of grid-side converter (GSC) controller, and other factors on the system stability have been analyzed by the eigenvalue method. Based on the small-signal model of the system, the basic principle of the impedance analysis method has been detailed in [4], and the stability criteria have been put forward. The *dq*-domain impedance model and the sequence impedance model have been introduced in [5], and the mechanism of instability has been revealed from the perspective of contributing negative resistance to the system. Although the above methods can realize the analysis of the system oscillation stability under small disturbances, they cannot be used to analyze the large disturbance stability of the system. The large disturbance stability can be analyzed by the equal area method, phase plane method, and energy function method. In [6]-[8], the large-disturbance stability of the grid-connected converter has been assessed by the equal area method, and it has been analyzed how phase-locked loop (PLL) parameters and critical clearing time affect the system stability. In [9]-[11], the projection theorem has been used by the phase plane method to project the high-dimensional motion equation of the system onto the low-dimensional phase plane so as to obtain the trajectory of the system, and then the large-disturbance stability of the system is assessed by analyz-

Manuscript received: March 5, 2024; revised: April 8, 2024; accepted: April 19, 2024. Date of CrossCheck: April 19, 2024. Date of online publication: May 10, 2024.

This work was supported by National Natural Science Foundation of China (No. 52130709).

J. Ma (corresponding author), N. Su, Y. Deng, H. Xu, and Y. Shen are with the State Key Laboratory of Alternate Electrical Power System with Renewable Energy Sources, North China Electric Power University, Beijing 102206, China (e-mail: hdmajing@163.com; hbsjzsns@163.com; 18810076770@163.com; deer136929789@163.com; jsntsyq1994@163.com).

W. Xia is with Shenyang Institute of Engineering, Shenyang, China (e-mail: 1571882670@qq.com).

DOI: 10.35833/MPCE.2024.000240

ing the convergence of different trajectories. The energy function method mentioned in [12] - [14] judges the large-disturbance stability of the system according to the convergence of the Lyapunov energy function. The stability analysis results of the above methods are relatively conservative, and the instability mechanism cannot be revealed [15], [16]. In [17] and [18], the energy model of the system considering the control links has been built, the effect of different control parameters on the stability of system has been analyzed, and the mechanism of instability has been revealed. Hence, the energy function method is suited in revealing the instability mechanism of the system.

The existing oscillation suppression strategies for grid-connected DFIG-based wind farms via VSC-HVDC transmission system primarily include control parameter optimization, additional damping controller, and control branch compensation. The parameter tuning strategy proposed in [19] and [20] suppresses the oscillation by maximizing the damping ratio of the system at the resonance point through optimization of the control parameters. This method cannot be applied online, and the range of parameter tuning is limited. The strategies of adding supplementary damping controller proposed in [21] and [22] realize the oscillation suppression in a specific frequency band by adding a supplementary damping control device. It has a significant suppression effect, but the supplementary damping device raises the cost and complexity of the system operation, even interacting with the DC converter that causes system instability. The control branch compensation strategy designs the damping control branch on the basis of the existing control system according to the characteristics of oscillation [23], [24]. It has fast response and a wide range of regulation.

To deal with the challenges in suppressing the oscillation in grid-connected DFIG-based wind farms via VSC-HVDC transmission system, a new oscillation suppression strategy is proposed in this paper. By constructing the energy model of the system and depicting the flow of dynamic energy in the system after fault clearance, the occurring and developing mechanism of the oscillation is revealed, and an oscillation suppression strategy is put forward. First, considering the dynamic characteristics of different control modules of grid-connected DFIG-based wind farms via VSC-HVDC transmission system, the system is divided into several subsystems, and the energy model of each subsystem is constructed. Then, the magnitude and direction of each interaction energy are calculated, and the key control links that magnify and transmit the interaction energy are identified. Furthermore, it is revealed that the *d*-axis subsystem of DFIG rotor-side converter (RSC) current inner loop, PLL, and the *q*-axis subsystem of VSC-HVDC voltage outer loop are the key links that induce the oscillation. On this basis, the corresponding supplementary control links are designed to suppress the transmission of the oscillation energy. Finally, a simulation model of grid-connected DFIG-based wind farms via VSC-HVDC transmission system is built in the RT-LAB experimental platform, on which the correctness and effectiveness of the proposed strategy are verified.

II. Dynamic Energy Modeling and Stability Analysis of Grid-connected DFIG-based Wind Farms via VSC-HVDC Transmission System

As shown in Fig. 1, a grid-connected DFIG-based wind farm via VSC-HVDC transmission system is composed of the DFIG, RSC, DC link, GSC, and VSC-HVDC converter station. In Fig. 1, PI is the proportional-integral controller.

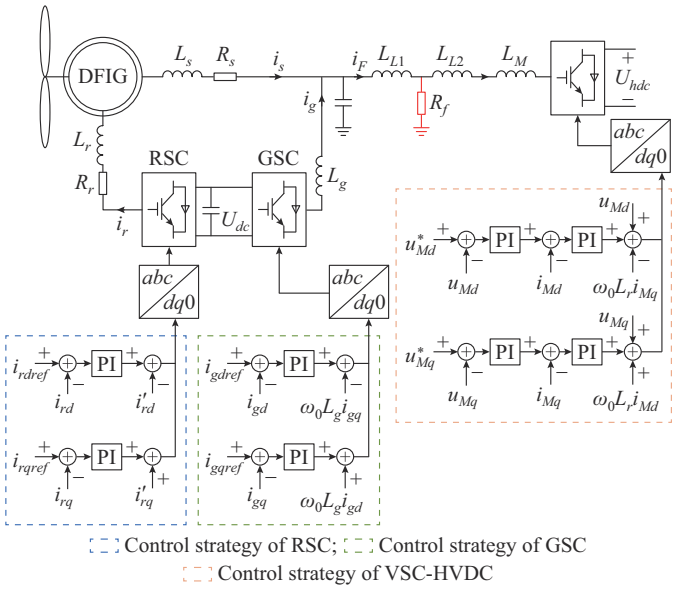

Fig. 1. Topology of grid-connected DFIG-based wind farm via VSC-HVDC transmission system.

Since the DC link of the VSC-HVDC transmission system has an isolating effect, the dynamic characteristic of the DFIG-side flexible DC converter station can represent the dynamic characteristic of the whole interconnected system.

A. Mathematical Model of Grid-connected DFIG-based Wind Farms via VSC-HVDC Transmission System

After a fault is cleared, the mathematical models of the grid-connected DFIG-based wind farms via VSC-HVDC transmission system are shown as follows.

The mathematical models for the subsystems of VSC-HVDC current inner loop are given as:

$$\begin{cases} C_{IIM}\dfrac{\mathrm{d}\Delta u_{IIMd}}{\mathrm{d}t} = -\Delta i_{Md} + T_{IIMd} \\ L_{IIM}\dfrac{\mathrm{d}\Delta i_{Md}}{\mathrm{d}t} = -R_{IIM}\Delta i_{Md} + \Delta u_{IIMd} + T_{iMd} \end{cases} \tag{1}$$

$$\begin{cases} C_{IIM}\dfrac{\mathrm{d}\Delta u_{IIMq}}{\mathrm{d}t} = -\Delta i_{Mq} + T_{IIMq} \\ L_{IIM}\dfrac{\mathrm{d}\Delta i_{Mq}}{\mathrm{d}t} = -R_{IIM}\Delta i_{Mq} + \Delta u_{IIMq} + T_{iMq} \end{cases} \tag{2}$$

where $R_{IIM}=K_{p1,VSC}$, $C_{IIM}=1/K_{i1,VSC}$, and $K_{p1,VSC}$ and $K_{i1,VSC}$ are the proportional and integral coefficients, respectively; $L_{IIM}=L_M$, and L_M is the equivalent inductance of VSC-HVDC converter; Δi_{Md} and Δi_{Mq} are the *d*-axis and *q*-axis variations of the output current of VSC-HVDC converter, respectively; $T_{iMd}=K_{p1,VSC}\Delta i^*_{Md}$, $T_{iMq}=K_{i1,VSC}\Delta i^*_{Mq}$, $T_{IIMd}=\Delta i^*_{Md}$, $T_{IIMq}=\Delta i^*_{Mq}$, and Δi^*_{Md} and Δi^*_{Mq} are the variations of the reference values

of i_{Md} and i_{Mq}, respectively; and Δu_{IIMd} and Δu_{IIMq} are the *d*-axis and *q*-axis output variations of the current inner loop integrator of the VSC-HVDC converter, respectively.

The mathematical models of RSC current inner loop subsystems are given as:

$$\begin{cases} C_{IIR}\dfrac{\mathrm{d}\Delta u_{IIRd}}{\mathrm{d}t} = -\Delta i_{rd} + T_{IIRd} \\ L_{IIR}\dfrac{\mathrm{d}\Delta i_{rd}}{\mathrm{d}t} = -R_{IIR}\Delta i_{rd} + \Delta u_{IIRd} + T_{ird} \end{cases} \tag{3}$$

$$\begin{cases} C_{IIR}\dfrac{\mathrm{d}\Delta u_{IIRq}}{\mathrm{d}t} = -\Delta i_{rq} + T_{IIRq} \\ L_{IIR}\dfrac{\mathrm{d}\Delta i_{rq}}{\mathrm{d}t} = -R_{IIR}\Delta i_{rq} + \Delta u_{IIRq} + T_{irq} \end{cases} \tag{4}$$

where $R_{IIR}=R_r+K_{p1,D}$, $C_{IIR}=1/K_{i1,D}$, R_r is the resistance of DFIG rotor windings, and $K_{p1,D}$ and $K_{i1,D}$ are the proportional and integral coefficients, respectively; $L_{IIR}=\sigma L_r/\left(1+k_\omega k_{11}k_{10}/\sigma_\omega\right)$, k_ω, k_{10}, k_{11}, σ_ω, and σ are all dimensionless constants, $k_\omega=\omega_{slip}/\left(\omega_0-1\right)$, $k_{10}=L_m/L_r$, $k_{11}=L_m/L_s$, $\sigma_\omega=1-\omega_{slip}L_m^2/\left(\omega_0 L_r L_s\right)$, $\sigma=1-L_m^2/\left(L_r L_s\right)$, L_r, L_s, and L_m are the rotor, stator, and mutual inductances, respectively, $\omega_{slip}=\left(\omega_0-\omega_r\right)/\omega_0$, ω_r is the rotor angular frequency, and $\omega_0=100\pi$; Δi_{rd} and Δi_{rq} are the *d*-axis and *q*-axis variations of DFIG rotor current, respectively; Δu_{IIRd} and Δu_{IIRq} are the *d*-axis and *q*-axis oscillation components of the output of RSC current inner loop integrators, respectively; $T_{IIRd}=\cos\Delta\theta\Delta i_{rd}^*-\sin\Delta\theta\Delta i_{rq}^*$, $T_{IIRq}=\sin\Delta\theta\Delta i_{rd}^*+\cos\Delta\theta\Delta i_{rq}^*$, $\Delta\theta$ is the angular difference between the power frequency coordinate system and the PLL coordinate system, and Δi_{rd}^* and Δi_{rq}^* are the variations of the reference values of i_{rd} and i_{rq}, respectively; and T_{ird} and T_{irq} are detailed in Supplementary Material A.

The mathematical model of PLL subsystem is given as:

$$\begin{cases} C_{pll}\dfrac{\mathrm{d}\Delta u_{I\omega}}{\mathrm{d}t} = -\Delta i_{I\theta} + T_{I\omega} \\ L_{pll}\dfrac{\mathrm{d}\Delta i_{I\theta}}{\mathrm{d}t} = \Delta u_{I\omega} - R_{pll}\Delta i_{I\theta} + T_{I\theta} \end{cases} \tag{5}$$

where $R_{pll}=K_{pllp}u_{sd,SEP}$, $C_{pll}=1/\left(K_{plli}u_{sd,SEP}\right)$, $L_{pll}=1$, K_{pllp} and K_{plli} are the proportional and integral coefficients, respectively, and $u_{sd,SEP}$ is the steady-state value of the *d*-axis voltage of DFIG stator; $\Delta u_{I\omega}$ and $\Delta i_{I\theta}$ are the variations of the angular velocity and angle of PLL, respectively; and $T_{I\omega}=\Delta u_{sq}/u_{sd,SEP}$, $T_{I\theta}=K_{pllp}\Delta u_{sq}$, and the expression for Δu_{sq} is detailed in Supplementary Material A.

The mathematical models of the subsystems of GSC voltage outer loop, GSC current inner loop, RSC power outer loop, VSC-HVDC voltage outer loop, and AC line are the same as those obtained in [25] and [26], and their derivation process is not repeated in this paper.

B. Energy Model of Grid-connected DFIG-based Wind Farms via VSC-HVDC Transmission System

The mathematical models of the subsystems of grid-connected DFIG-based wind farms via VSC-HVDC transmission system can be represented by the general formula in (6).

$$\begin{cases} C_k\dfrac{\mathrm{d}\Delta U}{\mathrm{d}t} = -\Delta I + T_U \\ L_k\dfrac{\mathrm{d}\Delta I}{\mathrm{d}t} = -R_k\Delta i + \Delta U + T_I \end{cases} \tag{6}$$

where R_k, L_k, and C_k are the resistance, inductance, and capacitance, respectively; and T_U and T_I are the interactions between different subsystems.

According to the first integration method illustrated in [27], integrating equation (6) along the time t can yield the energy model of the subsystem:

$$\frac{1}{2}C_k\Delta U^2+\frac{1}{2}L_k\Delta I^2+R_k\int\Delta I^2\mathrm{d}t-\int\left(T_I\Delta I+T_U\Delta U\right)\mathrm{d}t=Const \tag{7}$$

where $C_k\Delta U^2/2+L_k\Delta I^2/2$ represents the energy stored in the equivalent capacitance and inductance of the subsystem, which is referred to as V_p in this paper; $R_k\int\Delta I^2\mathrm{d}t$ represents the energy dissipated by the equivalent resistance, which is referred to as V_D in this paper; $-\int\left(T_I\Delta I+T_U\Delta U\right)\mathrm{d}t$ represents the interaction energy between the subsystems, which is referred to as V_T in this paper; and *Const* is a constant.

The dynamic energy model of each subsystem can be obtained by applying (1)-(5) to (7), as shown in (8)-(12). The dynamic energy models of VSC-HVDC current inner loop subsystems are given as (8) and (9). The dynamic energy model of PLL subsystem is given as (10). The dynamic energy models of RSC current inner loop subsystems are given as (11) and (12).

$$\frac{1}{2}C_{IIM}\Delta u_{IIMd}^2+\frac{1}{2}L_{IIM}\Delta i_{Md}^2+R_{IIM}\int\Delta i_{Md}^2\mathrm{d}t+\int\Delta i_{Md}^*\Delta u_{IIMd}\mathrm{d}t-R_{IIM}\int\Delta i_{Md}^*\Delta i_{Md}\mathrm{d}t=Const \tag{8}$$

$$\frac{1}{2}C_{IIM}\Delta u_{IIMq}^2+\frac{1}{2}L_{IIM}\Delta i_{Mq}^2+R_{IIM}\int\Delta i_{Mq}^2\mathrm{d}t+\int\Delta i_{Mq}^*\Delta u_{IIMq}\mathrm{d}t-R_{IIM}\int\Delta i_{Mq}^*\Delta i_{Mq}\mathrm{d}t=Const \tag{9}$$

$$\begin{aligned}&\frac{1}{2}C_{pll}\Delta u_{I\omega}^2+\frac{1}{2}L_{pll}\Delta i_{I\theta}^2+R_{pll}\int\Delta i_{I\theta}^2\mathrm{d}t+\frac{K_{pllp}k_{10}}{\sigma_\omega}\left[\frac{\sigma\omega_0L_r}{k_{11}}\int\Delta i_{sd}\Delta i_{I\theta}\mathrm{d}t-\frac{k_{14}\sigma}{k_{11}}\int\Delta u_{IIMq}\Delta i_{I\theta}\mathrm{d}t+\frac{K_{p1,VSC}k_{14}\sigma}{k_{11}}\int\Delta i_{Mq}^*\Delta i_{I\theta}\mathrm{d}t-\right.\\&\left.\int\Delta u_{IIRq}\Delta i_{I\theta}\mathrm{d}t+\left(R_r+K_{p1,D}\right)\int\Delta i_{rq}\Delta i_{I\theta}\mathrm{d}t-K_{p1,D}\int\Delta i_{rq}^*\Delta i_{I\theta}\mathrm{d}t+\left(\frac{R_s}{k_{10}}-\frac{K_{p1,VSC}k_{14}\sigma}{k_{11}}\right)\int\Delta i_{sq}\Delta i_{I\theta}\mathrm{d}t+\left(\omega_{slip}-\omega_0\right)L_ra\int\Delta i_{rd}\Delta i_{I\theta}\mathrm{d}t\right]+\\&\frac{k_{10}}{\sigma_\omega u_{sd,SEP}}\left[\left(\frac{R_s}{k_{10}}-\frac{K_{p1,VSC}k_{14}\sigma}{k_{11}}\right)\int\Delta i_{sq}\Delta u_{I\omega}\mathrm{d}t+\frac{\sigma\omega_0L_r}{k_{11}}\int\Delta i_{sd}\Delta u_{I\omega}\mathrm{d}t-\int\Delta u_{IIRq}\Delta u_{I\omega}\mathrm{d}t-\frac{k_{14}\sigma}{k_{11}}\int\Delta u_{IIMq}\Delta u_{I\omega}\mathrm{d}t-K_{p1,D}\int\Delta i_{rq}^*\Delta u_{I\omega}\mathrm{d}t+\right.\\&\left.\frac{K_{p1,VSC}k_{14}\sigma}{k_{11}}\int\Delta i_{Mq}^*\Delta u_{I\omega}\mathrm{d}t\left(R_r+K_{p1,D}\right)\int\Delta i_{rq}\Delta u_{I\omega}\mathrm{d}t+\left(\omega_{slip}-\omega_0\right)L_r\int\Delta i_{rd}\Delta u_{I\omega}\mathrm{d}t\right]=Const\end{aligned} \tag{10}$$

$$\frac{1}{2}C_{IIR}\Delta u_{IIRd}^2+\frac{1}{2}L_{IIR}\Delta i_{rd}^2+R_{IIR}\int\Delta i_{rd}^2\mathrm{d}t-\frac{\sigma_\omega}{k_\omega k_{11}k_{10}+\sigma_\omega}\cdot\left\{\frac{K_{p1,D}\left(k_\omega k_{10}k_{11}+\sigma_\omega\right)}{\sigma_\omega}\int\left(\Delta i_{rd}^*\Delta i_{rd}-\Delta i_{rq}^*\Delta i_{rd}\Delta i_{I\theta}\right)\mathrm{d}t-\left[\frac{k_\omega k_{11}\left(\omega_0-\omega_{slip}\right)L_m}{\sigma_\omega}-\omega_{slip}\sigma_{\omega 2}L_r\right]\int\Delta i_{rq}\Delta i_{rd}\mathrm{d}t-\left[\frac{\left(k_\omega+\sigma_\omega\right)k_{11}R_s}{\sigma_\omega}-\frac{K_{p1,VSC}k_\omega k_9k_{11}\sigma}{\sigma_\omega}\right]\int\Delta i_{Md}\Delta i_{rd}\mathrm{d}t+\left[k_\omega k_{11}\omega_0L_s+\left(\omega_0-\omega_{slip}\right)L_m\right]\int\Delta i_{Mq}\Delta i_{rd}\mathrm{d}t+\frac{k_\omega k_9k_{11}\sigma}{\sigma_\omega}\int\Delta u_{IIMd}\Delta i_{rd}\mathrm{d}t-\frac{K_{p1,VSC}k_\omega k_9k_{11}\sigma}{\sigma_\omega}\int\Delta i_{Md}^*\Delta i_{rd}\mathrm{d}t\right\}-\left(\int\Delta i_{rd}^*\Delta u_{IIRd}dt-\int\Delta i_{rq}^*\Delta u_{IIRd}\Delta i_{I\theta}dt\right)=Const \tag{11}$$

$$\frac{1}{2}C_{IIR}\Delta u_{IIRq}^2+\frac{1}{2}L_{IIR}\Delta i_{rq}^2+R_{IIR}\int\Delta i_{rq}^2\mathrm{d}t-\frac{\sigma_\omega}{k_\omega k_{11}k_{10}+\sigma_\omega}\cdot\left\{\frac{K_{p1,D}\left(k_\omega k_{11}k_{10}+\sigma_\omega\right)}{\sigma_\omega}\int\left(\Delta i_{rq}^*\Delta i_{rq}+\Delta i_{rq}^*\Delta i_{rq}\Delta i_{I\theta}\right)\mathrm{d}t-\left[\frac{k_\omega k_{11}\left(\omega_{slip}-\omega_0\right)L_m}{\sigma_\omega}+\omega_{slip}\sigma_{\omega 2}L_r\right]\int\Delta i_{rq}\Delta i_{rd}\mathrm{d}t-\left[\frac{\left(k_\omega+\sigma_\omega\right)k_{11}R_s}{\sigma_\omega}-\frac{K_{p1,VSC}k_\omega k_9k_{11}\sigma}{\sigma_\omega}\right]\int\Delta i_{Mq}\Delta i_{rq}\mathrm{d}t+\left[k_\omega k_{11}\omega_0L_s+\left(\omega_0-\omega_{slip}\right)L_m\right]\int\Delta i_{Md}\Delta i_{rq}\mathrm{d}t+\frac{k_\omega k_9k_{11}\sigma}{\sigma_\omega}\int\Delta u_{IIMq}\Delta i_{rq}\mathrm{d}t-\frac{K_{p1,VSC}k_\omega k_9k_{11}\sigma}{\sigma_\omega}\int\Delta i_{Mq}^*\Delta i_{rq}\mathrm{d}t\right\}-\left(\int\Delta i_{rd}^*\Delta u_{IIRq}\mathrm{d}t-\int\Delta i_{rq}^*\Delta u_{IIRq}\Delta i_{I\theta}\mathrm{d}t\right)=Const \tag{12}$$

where $k_{14}=L_r/L_M$; k_9 and $\sigma_{\omega 2}$ are dimensionless constants; and Δi_{sd} and Δi_{sq} are the variations of d-axis and q-axis output currents of DFIG, respectively.

C. Analysis of Interaction Path of Oscillation Based on Dynamic Energy Flow

Based on the relationship between the stored energy and system stability [18], when the system is disturbed, it is asymptotically stable if the stored energy V_P decreases with time and eventually reaches its minimum. Meanwhile, if V_P increases with time, the system will be destabilized. Therefore, the system stability can be reflected by the variation trend of V_P.

From (7), the derivatives of V_P, V_D, and V_T satisfy:

$$\dot{V}_P=-\dot{V}_D-\dot{V}_T \tag{13}$$

It can be observed from (7) that $\dot{V}_D$ is constantly positive, so it has negative contribution to $\dot{V}_P$. In other words, $\dot{V}_D$ can help the system remain stable. When $-\dot{V}_T>0$, $-\dot{V}_T$ has positive contribution to $\dot{V}_P$, meaning that the interaction energy will cause the system instability. When $-\dot{V}_T<0$, $-\dot{V}_T$ has negative contribution to $\dot{V}_P$, meaning that the interaction energy will help the system remain stable. And the oscillation transmission path can be depicted by analyzing the interaction energy between different subsystems.

Assume that an oscillation with constant amplitude occurs in the grid-connected DFIG via VSC-HVDC transmission system after the fault is cleared, with the dominant oscillation component of DFIG output current being $G_{is}e^{j\beta t}$. G_{is} is the amplitude of the current variation. In this case, the oscillation components of state variables in each subsystem can be written according to (1)-(5), as shown in (14).

$$\begin{cases}\Delta i_{sd}+\mathrm{j}\Delta i_{sq}=\Delta i_{Md}+\mathrm{j}\Delta i_{Mq}=G_{is}e^{\mathrm{j}\gamma t}\\ \Delta i_{rd}+\mathrm{j}\Delta i_{rq}=G_{ir}e^{\mathrm{j}\left(\gamma t+\phi_{ir}\right)}\\ \Delta u_{sq}=G_{us}\sin\left(\gamma t+\phi_{us}\right)\\ \Delta u_{IIRd}+\mathrm{j}\Delta u_{IIRq}=G_{uIIR}e^{\mathrm{j}\left(\gamma t+\phi_{uIIR}\right)}\\ \Delta u_{IIMd}+\mathrm{j}\Delta u_{IIMq}=G_{uIIM}e^{\mathrm{j}\left(\gamma t+\phi_{uIIM}\right)}\\ \Delta u_{I\omega}=G_{I\omega}\cos\left(\gamma t+\phi_{I\omega}\right)\\ \Delta i_{I\theta}=G_{I\theta}\cos\left(\gamma t+\phi_{I\theta}\right)\end{cases} \tag{14}$$

where G_{ir}, G_{us}, G_{uIIR}, G_{uIIM}, $G_{I\omega}$, $G_{I\theta}$ and ϕ_{ir}, ϕ_{us}, ϕ_{uIIR}, ϕ_{uIIM}, $\phi_{I\omega}$, $\phi_{I\theta}$ are the amplitudes and phases of the variations of DFIG rotor current, DFIG stator voltage, RSC inner loop integrator output, VSC-HVDC inner loop integrator output, output angular velocity of PLL, and output phase of PLL, respectively; and γ is the angular velocity of the oscillation.

By applying (14) to the energy model of each subsystem shown in (8) - (12), the expressions for different interaction energy items between different subsystems can be obtained.

1) Interaction Energy Links of d-axis Subsystem and q-axis Subsystem of VSC-HVDC Current Inner Loop: AC Line

According to the energy model of the grid-connected DFIG-based wind farms via VSC-HVDC transmission system, there are four interaction energy items between the two subsystems and others, i.e., ① $V_{T,C1w}$ and $V_{T,L1w}$, which are the interaction energies flowing from d-axis subsystem of VSC-HVDC voltage outer loop to d-axis subsystem of VSC-HVDC current inner loop on the AC line; ② $V_{T,C2w}$ and $V_{T,L2w}$, which are the interaction energies flowing from q-axis subsystem of VSC-HVDC voltage outer loop to q-axis subsystem of VSC-HVDC current inner loop on the AC line. The expressions for $\dot{V}_{T,C1w}$, $\dot{V}_{T,L1w}$, $\dot{V}_{T,C2w}$, and $\dot{V}_{T,L2w}$ are:

$$\begin{cases}\dot{V}_{T,C1w}=\dfrac{G_{iM^*}G_{uIIM}}{2}\left(\cos\left(\phi_{uIIM}-\phi_{iM^*}\right)+\cos\left(2\gamma t+\phi_{uIIM}+\phi_{iM^*}\right)\right)\\ \dot{V}_{T,L1w}=\dfrac{K_{p1,VSC}G_{iM^*}G_{iM}}{2}\left(-\cos\left(\phi_{iM}-\phi_{iM^*}\right)-\cos\left(2\gamma t+\phi_{iM}+\phi_{iM^*}\right)\right)\\ \dot{V}_{T,C2w}=\dfrac{G_{iM^*}G_{uIIM}}{2}\left(\cos\left(\phi_{uIIM}-\phi_{iM^*}\right)-\cos\left(2\gamma t+\phi_{uIIM}+\phi_{iM^*}\right)\right)\\ \dot{V}_{T,L2w}=\dfrac{K_{p1,VSC}G_{iM^*}G_{iM}}{2}\left(-\cos\left(\phi_{iM}-\phi_{iM^*}\right)+\cos\left(2\gamma t+\phi_{uIIM}+\phi_{iM^*}\right)\right)\end{cases} \tag{15}$$

where G_{iM} and ϕ_{iM} are the amplitude and phase variations of the VSC-HVDC converter output current, respectively; and

G_{iM*} and ϕ_{iM*} are the reference values of G_{iM} and ϕ_{iM}, respectively. From (15), $\dot{V}_{T,C1w}$, $\dot{V}_{T,L1w}$, $\dot{V}_{T,C2w}$, and $\dot{V}_{T,L2w}$ vary periodically. Therefore, the stored energy of VSC-HVDC voltage outer loop and current inner loop also varies periodically, and the oscillation will go on. Since $\cos\left(\phi_{iM*}-\phi_{uIIM}\right)\approx 0$, $\cos\left(\phi_{iM*}-\phi_{iM}\right)\approx 0$, the accumulated values of $V_{T,C1w}$, $V_{T,L1w}$, $V_{T,C2w}$, and $V_{T,L2w}$ are all 0 within one oscillation period. It means that this interaction only transmits the oscillation, and will not change the stored energy of the system.

2) Interaction Energy Links of d-axis Subsystem and q-axis Subsystem of RSC Current Inner Loop: DFIG Rotor

There are eighteen interaction energy items between the two subsystems and others, i.e., ① $V_{T,C53}$ and $V_{T,C3w3}$ are the interaction energies flowing from RSC outer loop subsystem and PLL to the *d*-axis subsystem, respectively; ② $V_{T,L23}$, $V_{T,L1C3}$, $V_{T,L13}$, $V_{T,L53}$, $V_{T,L1w3}$, $V_{T,L43}$, and $V_{T,L3w3}$ are the interaction energies flowing from PLL, VSC-HVDC voltage outer loop subsystem, VSC-HVDC current inner loop subsystems, RSC inner loop subsystem, and outer loop subsystem to the *d*-axis subsystem, respectively. The expressions for $\dot{V}_{T,C53}$, $\dot{V}_{T,C3w3}$, $\dot{V}_{T,L23}$, $\dot{V}_{T,L53}$, $\dot{V}_{T,L1w3}$, $\dot{V}_{T,L43}$, $\dot{V}_{T,L1C3}$, $\dot{V}_{T,L13}$, and $\dot{V}_{T,L3w3}$ are given in Supplementary Material A. Similarly, the interaction energy between the *q*-axis subsystem and others is also given in the Supplementary Material A.

Applying the amplitude-phase analysis method, within the sub-/super-synchronous frequency ranges, $-\dot{V}_{T,L13}>0$, and the magnitude of $\left|\dot{V}_{T,L13}\right|$ is far greater than the others. Similarly, $-\dot{V}_{T,L24}<0$, $-\dot{V}_{T,L2w4}>0$, and the magnitudes of $\left|\dot{V}_{T,L2w4}\right|$ and $\left|\dot{V}_{T,L24}\right|$ are far greater than the others. Thus, $V_{T,L24}$, $V_{T,L13}$, and $V_{T,L2w4}$ are the dominant interaction energy items. The detailed analysis and derivation process are given in Supplementary Material B.

3) Interaction Energy Links of PLL

There are eight interaction energy items between state variables of PLL $i_{I\theta}$ and other subsystems, i.e., $\dot{V}_{T,\theta 25}$, $\dot{V}_{T,\theta 2C5}$, $\dot{V}_{T,\theta 2w5}$, $V_{T,\theta 15}$, $\dot{V}_{T,\theta 45}$, $\dot{V}_{T,\theta 4C5}$, $V_{T,\theta 4w5}$, and $\dot{V}_{T,\theta 35}$, which are the interaction energies flowing from VSC-HVDC voltage outer loop subsystems, VSC-HVDC current inner loop subsystems, RSC outer loop subsystems, and RSC current inner loop subsystems to PLL. Similarly, there are also eight interaction energy items between state variable of PLL $u_{I\omega}$ and other subsystems, as shown in (9).

According to the amplitude-phase analysis method, within the sub-/super-synchronous frequency ranges, $\left|\dot{V}_{T,\theta 35}\right|$, $\left|\dot{V}_{T,w25}\right|$, $\left|\dot{V}_{T,w4w5}\right|$, $\left|\dot{V}_{T,w2w5}\right|$, and $\left|\dot{V}_{T,w45}\right|$ are far greater than the others, and $-\dot{V}_{T,w4w5}<0$, $-\dot{V}_{T,w2w5}>0$, $-\dot{V}_{T,w45}>0$, $-\dot{V}_{T,w25}<0$, $-\dot{V}_{T,\theta 35}>0$. Thus, $V_{T,\theta 35}$, $V_{T,w25}$, $V_{T,w2w5}$, $V_{T,w4w5}$, and $V_{T,w45}$ are the dominant interaction energy items in the above interaction energy items. The detailed analysis and derivation process can be found in Supplementary Material C.

D. Analysis of System Oscillation Stability Based on Dynamic Energy Flow

Based on the analysis in previous subsections, the oscillation interaction path of the grid-connected DFIG via VSC-HVDC transmission system can be depicted, as shown in Fig. 2. According to (13), when the derivative of the sum of the interaction energies between different subsystems $-\dot{V}_{T,s}>0$, the stored energy of the system is increasing with time, and the system is unstable. Similarly, when $-\dot{V}_{T,s}<0$, the stored energy of the system decreases with time, and the system remains stable.

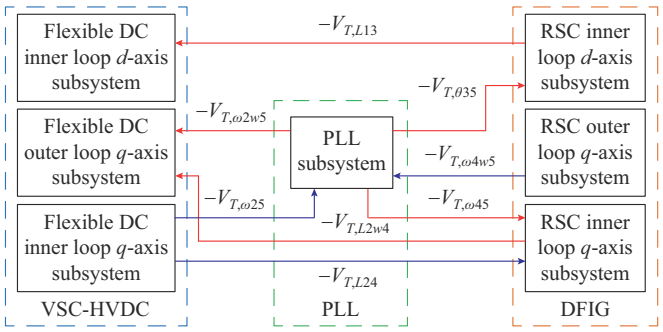

Fig. 2. Interaction path of oscillation in interconnected system.

The interaction energies $-V_{T,L13}$, $-V_{T,L2w4}$, $V_{T,\theta 35}$, $-V_{T,w2w5}$, and $-V_{T,w45}$ are all positive values increasing with time, while $-V_{T,w25}$, $-V_{T,L24}$, and $-V_{T,w4w5}$ are the negative values decreasing with time, and the sum of the above interaction energies is greater than 0 and increases with time. So, the stored energy of the system is increasing, and the system is unstable.

In Fig. 2, the interaction paths between different subsystems are marked in different colors, where the energy links in red indicate that the energy flows are not conducive to the system stability, while the energy links in blue indicate that the energy flows are conducive to the system stability. In addition, it can be observed from Fig. 2 that PLL is the main cause of system oscillation.

III. Oscillation Suppression Strategy

Based on the influences of different interaction energy links on the system stability, the interaction links can be classified into "transmitting links", "gaining links", and "damping links". Then, the key interaction links that induce the oscillation can be located. On this basis, corresponding compensation branches can be designed to suppress the oscillation.

A. RSC Phase Compensation Branch

After fault clearance, the oscillation in the grid-connected DFIG via VSC-HVDC transmission system is induced by the energy interaction between *q*-axis subsystem of RSC current inner loop and PLL, and the key interaction energy links are $-\dot{V}_{T,L89}=k_{10}/\sigma_{\omega}K_{pllp}\left(R_r+K_{irp}\right)\Delta i_{rq}\Delta u_{I\omega}$, $-\dot{V}_{T,L98}=K_{p1,D}\Delta i_{rd}^{*}\Delta i_{rq}\Delta\theta$, where $\Delta\theta=\Delta i_{I\theta}$. By adding two phase compensation branches to these dominant interaction links, the transmission of oscillation energy between RSC and PLL can be suppressed, as shown in Fig. 3.

After adding the phase compensation branch, the reference value vector of RSC inner loop moves an angle of $-\Delta\theta$ in the forward direction. This compensates for the difference between the reference value and measured value of the current resulting from the output deviation of PLL phase angle. The interaction energies of *d*-axis subsystem and *q*-axis subsystem of RSC current inner loop after the phase compensation are shown in (16) and (17), respectively.

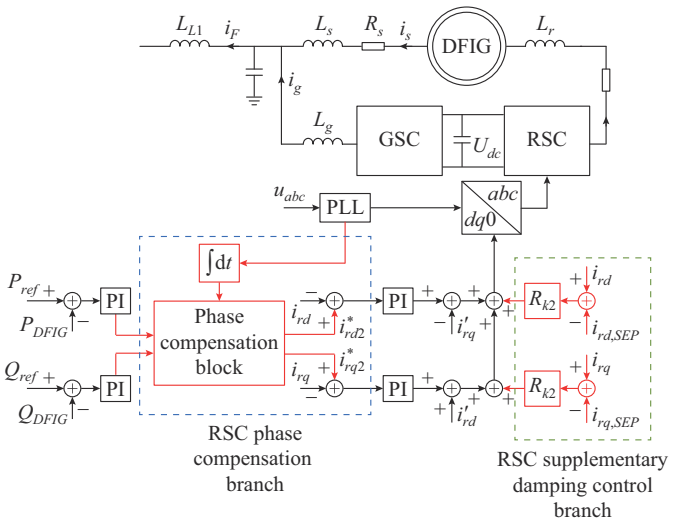

Fig. 3. Supplementary control links for oscillation suppression.

$$-\frac{\mathrm{d}V_{T2,IRd}}{\mathrm{d}t}=T_{ir2d}\Delta i_{rd}+T_{IIR2d}\Delta u_{IIRd}=\Delta i_{rd}^{*}\Delta u_{IIRd}+\frac{\sigma_\omega}{k_\omega k_{10}k_{11}+\sigma_\omega}\left\{\left[k_\omega k_{11}\omega_0 L_s+\left(\omega_0-\omega_{slip}\right)L_m\right]\Delta i_{sq}\Delta i_{rd}-\left[\frac{k_\omega k_{11}\left(\omega_0-\omega_{slip}\right)L_m}{\sigma_\omega}-\omega_{slip}\sigma_{\omega 2}L_r\right]\Delta i_{rq}\Delta i_{rd}+\frac{\left(k_\omega k_{10}k_{11}+\sigma_\omega\right)K_{p1,D}}{\sigma_\omega}\Delta i_{rd}^{*}\Delta i_{rd}-\left[\frac{\left(k_\omega+\sigma_\omega\right)k_{11}R_s}{\sigma_\omega}-\frac{K_{p1,VSC}k_\omega k_9 k_{11}\sigma}{\sigma_\omega}\right]\Delta i_{sd}\Delta i_{rd}+\frac{k_\omega k_9 k_{11}\sigma}{\sigma_\omega}\Delta u_{IIMd}\Delta i_{rd}-\frac{K_{p1,VSC}k_\omega k_9 k_{11}\sigma}{\sigma_\omega}\Delta i_{Md}^{*}\Delta i_{rd}\right\} \tag{16}$$

$$-\frac{\mathrm{d}V_{T2,IRq}}{\mathrm{d}t}=T_{ir2q}\Delta i_{rq}+T_{IIR2q}\Delta u_{IIRq}=\Delta i_{rq}^{*}\Delta u_{IIRq}+\frac{\sigma_\omega}{k_\omega k_{10}k_{11}+\sigma_\omega}\left\{\left[\frac{k_\omega k_{11}\left(\omega_0-\omega_{slip}\right)L_m}{\sigma_\omega}-\omega_{slip}\sigma_{\omega 2}L_r\right]\Delta i_{rd}\Delta i_{rq}+\frac{\left(k_\omega k_{10}k_{11}+\sigma_\omega\right)K_{p1,D}}{\sigma_\omega}\Delta i_{rq}^{*}\Delta i_{rq}-\left[\frac{\left(k_\omega+\sigma_\omega\right)k_{11}R_s}{\sigma_\omega}-\frac{K_{p1,VSC}k_\omega k_9 k_{11}\sigma}{\sigma_\omega}\right]\Delta i_{sq}\Delta i_{rq}-\left[\omega_0 k_\omega k_{11}L_s+\left(\omega_0-\omega_{slip}\right)L_m\right]\Delta i_{sd}\Delta i_{rq}+\frac{k_\omega k_9 k_{11}\sigma}{\sigma_\omega}\Delta u_{IIMq}\Delta i_{rq}-\frac{K_{p1,VSC}k_\omega k_9 k_{11}\sigma}{\sigma_\omega}\Delta i_{Mq}^{*}\Delta i_{rq}\right\} \tag{17}$$

Comparing (10), (11), (16), and (17), after the phase compensation, the interaction energies flowing from PLL to RSC current inner loop subsystems disappear. It means that the energy transmission between these subsystems can be blocked by the phase compensation branches.

When the system operates in normal state, $\Delta\theta=0$; thus, $i_{rd}^{*}\cos 0+i_{rq}^{*}\sin 0=i_{rd}^{*}$, $i_{rq}^{*}\cos 0-i_{rd}^{*}\sin 0=i_{rq}^{*}$, and the equations for RSC current inner loop will be those shown in (3) and (4). Therefore, the phase compensation branches will not affect the control performance of the system in normal operation state.

B. RSC Supplementary Damping Control Branch

Based on the above analysis, the subsystem of *d*-axis RSC current inner loop is the oscillation source and the key link that transmits oscillation energy to the output current of the wind farm. By increasing the dissipation energy of this subsystem, the cyclic process of gaining and transmitting oscillation energy can be effectively suppressed. After the supplementary damping branch is added, the control strategy of RSC inner loop becomes:

$$\frac{\sigma_\omega\sigma L_r}{k_\omega k_{10}k_{11}+\sigma_\omega}\frac{\mathrm{d}\Delta i_{rd}}{\mathrm{d}t}=-\left(R_r+K_{p1,D}\right)\Delta i_{rd}-R_{k2}\Delta i_{rd}+\Delta u_{IIRd}+\frac{\sigma_\omega}{k_\omega k_{10}k_{11}+\sigma_\omega}\left\{\frac{k_\omega k_9 k_{11}\sigma}{\sigma_\omega}\Delta u_{IIMd}-\frac{K_{p1,VSC}k_\omega k_9 k_{11}\sigma}{\sigma_\omega}\Delta i_{Md}^{*}-\left[\frac{k_\omega k_{11}\left(\omega_0-\omega_{slip}\right)L_m}{\sigma_\omega}-\sigma_{\omega 2}\omega_{slip}L_r\right]\Delta i_{rq}+\frac{\left(k_\omega k_{10}k_{11}+\sigma_\omega\right)K_{p1,D}}{\sigma_\omega}\left(\Delta i_{rd}^{*}\cos\Delta\theta-\Delta i_{rq}^{*}\sin\Delta\theta\right)-\frac{\left(k_\omega+\sigma_\omega\right)k_{11}R_s-K_{p1,VSC}k_\omega k_9 k_{11}\sigma}{\sigma_\omega}\Delta i_{sd}+\left[k_\omega k_{11}\omega_0 L_s+\left(\omega_0-\omega_{slip}\right)L_m\right]\Delta i_{sq}\right\} \tag{18}$$

$$\frac{\sigma_\omega\sigma L_r}{k_\omega k_{10}k_{11}+\sigma_\omega}\frac{\mathrm{d}\Delta i_{rq}}{\mathrm{d}t}=-\left(R_r+K_{p1,D}\right)\Delta i_{rq}-R_{k2}\Delta i_{rq}+\Delta u_{IIRq}+\frac{\sigma_\omega}{\sigma_\omega+k_\omega k_{10}k_{11}}\left\{\frac{k_\omega k_9 k_{11}\sigma}{\sigma_\omega}\Delta u_{IIMq}-\frac{K_{p1,VSC}k_\omega k_9 k_{11}\sigma}{\sigma_\omega}\Delta i_{Mq}^{*}+\left[\frac{k_\omega k_{11}\left(\omega_0-\omega_{slip}\right)L_m}{\sigma_\omega}-\sigma_{\omega 2}\omega_{slip}L_r\right]\Delta i_{rd}+\frac{\left(k_\omega k_{10}k_{11}+\sigma_\omega\right)K_{p1,D}}{\sigma_\omega}\left(\Delta i_{rd}^{*}\sin\Delta\theta+\Delta i_{rq}^{*}\cos\Delta\theta\right)-\frac{\left(k_\omega+\sigma_\omega\right)k_{11}R_s-K_{p1,VSC}k_\omega k_9 k_{11}\sigma}{\sigma_\omega}\Delta i_{sq}-\left[k_\omega k_{11}\omega_0 L_s+\left(\omega_0-\omega_{slip}\right)L_m\right]\Delta i_{sd}\right\} \tag{19}$$

where R_{k2} is the control parameter for the supplementary damping control branch, and the value of R_{k2} is 0.5.

The dissipation energy of the subsystem becomes:

$$\frac{\mathrm{d}V_{D2,IIRd}}{\mathrm{d}t}=V_{D2,IIRd}+\Delta V_{D2,IIRd,k2}=\int R_{IIR}\Delta i_{rd}^{2}\mathrm{d}t+\int R_{k2}\Delta i_{rd}^{2}\mathrm{d}t \tag{20}$$

$$\frac{\mathrm{d}V_{D2,IIRq}}{\mathrm{d}t}=V_{D2,IIRq}+\Delta V_{D2,IIRq,k2}=\int R_{IIR}\Delta i_{rq}^{2}\mathrm{d}t+\int R_{k2}\Delta i_{rq}^{2}\mathrm{d}t \quad (21)$$

As can be observed from (20) and (21), a positive increment is added to the dissipation energy of the RSC current inner loop subsystems after the supplementary damping control branch is added. Since the energy dissipation intensity of the subsystem increases, the energy dissipation intensity of the whole system also increases.

When the system operates in the steady state, the deviation of rotor current from the equilibrium point will be 0, and the supplementary damping control branch $-R_{k2}\Delta i_{rd}$ will be 0. Therefore, the supplementary damping control branch will not affect the system control performance in the normal operation state.

IV. Simulation Verification

A simulation model of the grid-connected DFIG-based wind farms via VSC-HVDC transmission system is built on the RT-LAB platform, as shown in Fig. 4, and the main simulation parameters are shown in Table I.

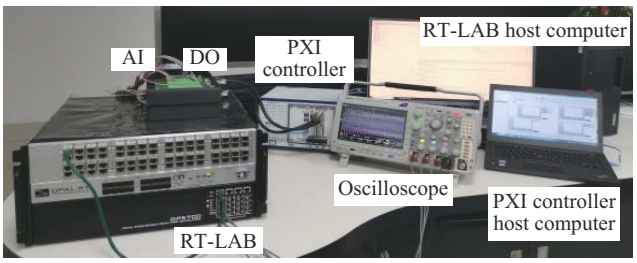

Fig. 4. Hardware-in-loop experiment platform.

In the above experiment system, a three-phase ground fault is set to occur at $t=10.1$ s, then the system switches to the low voltage ride-through (LVRT) state. After 100 ms, the fault is cleared, and then the system topology returns to normal. The flexible DC converter returns to the constant voltage constant frequency control, and DFIG returns to the maximum power point tracking (MPPT) control.

TABLE I
Main Simulation Parameters of Grid-connected DFIG-based Wind Farms via VSC-HVDC Transmission System

Item	Parameter	Value
DFIG	Rotor inductance	0.16 p.u.
	Stator inductance	0.18 p.u.
PLL	Proportion coefficient	1.63
	Integration coefficient	40
RSC	Outer loop proportional coefficient	5
	Outer loop integral coefficient	50
	Inner loop proportional coefficient	0.6
	Inner loop integral coefficient	8
GSC	Outer loop proportional coefficient	8
	Outer loop integral coefficient	400
	Inner loop proportional coefficient	4
	Inner loop integral coefficient	50
Flexible DC converter station	Outer loop proportional coefficient	1
	Outer loop integral coefficient	25
	Inner loop proportional coefficient	1
	Inner loop integral coefficient	6

A. Verification of Effectiveness of Proposed Strategy

In the above three-phase ground fault scenario, the simulation results of DFIG output current, output active power, and voltage at point of common coupling (PCC) are shown in Fig. 5.

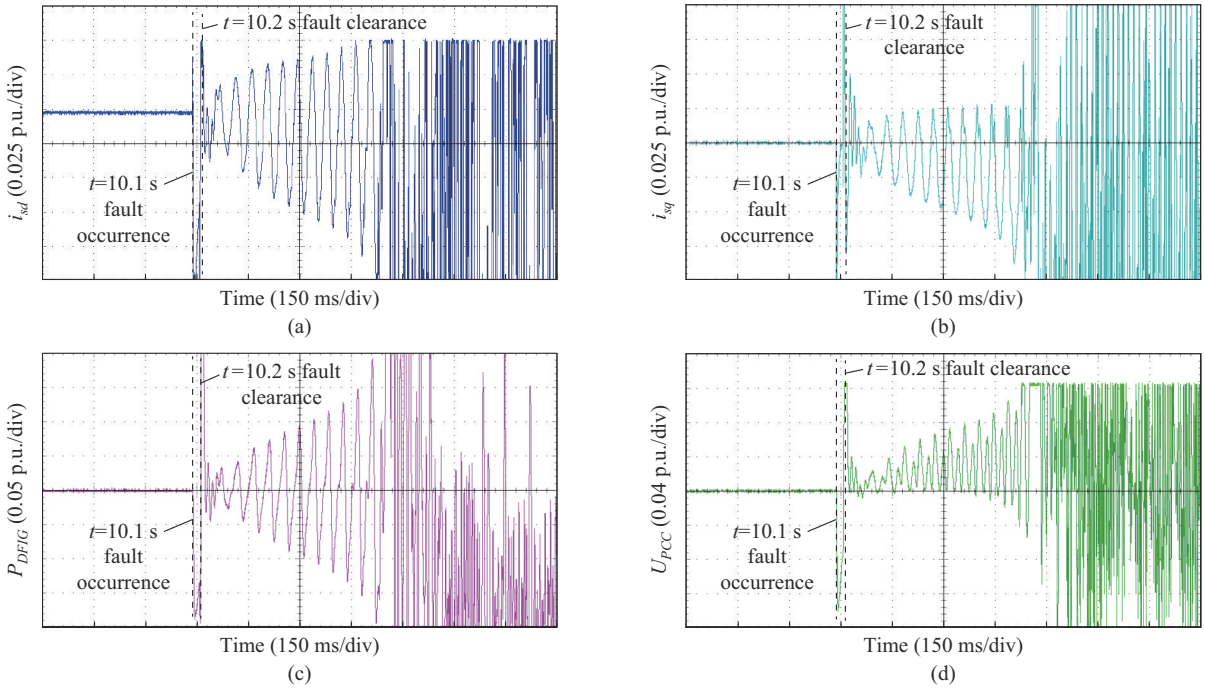

Fig. 5. Simulation results of DFIG output current, output active power, and voltage at PCC. (a) *d*-axis component of DFIG output current. (b) *q*-axis component of DFIG output current. (c) DFIG output active power. (d) Voltage at PCC.

According to Fig. 5, the oscillation in grid-connected DFIG-based wind farms via VSC-HVDC transmission system diverges after the fault is cleared. The simulation results of the interaction energy in Fig. 2 are obtained, as shown in Fig. 6.

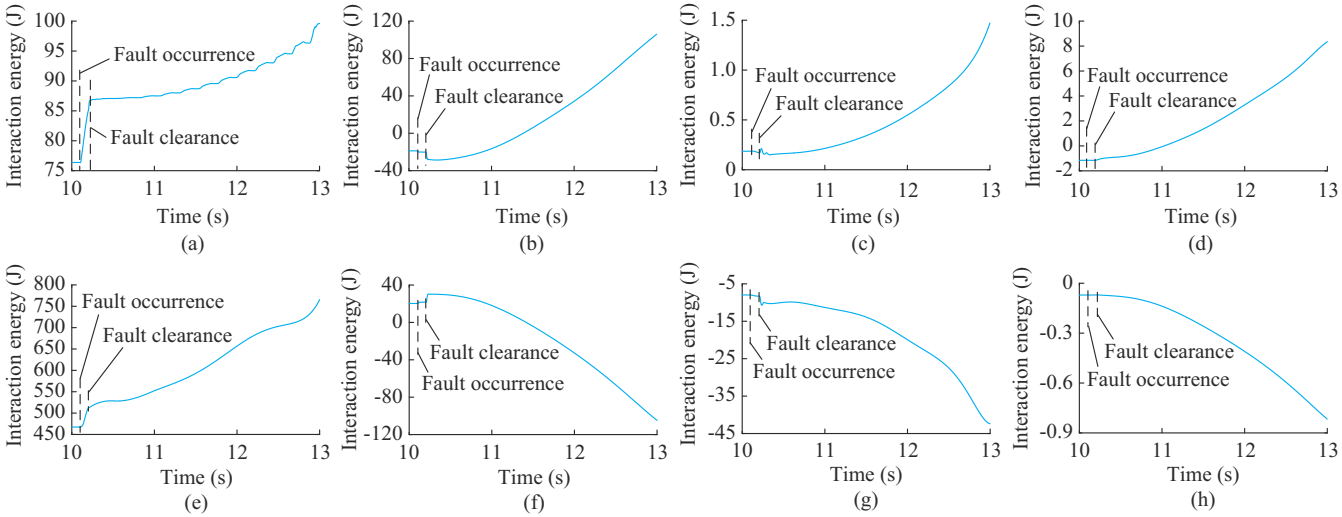

Fig. 6. Change of interaction energy during divergent oscillation. (a) $-V_{T,L13}$. (b) $-V_{T,L2w4}$. (c) $-V_{T,w45}$. (d) $-V_{T,w2w5}$. (e) $-V_{T,\theta 35}$.(f) $-V_{T,L24}$. (g) $-V_{T,w25}$. (h) $-V_{T,w4w5}$.

From Fig. 6(a)-(e), the magnitudes of $-V_{T,L13}$, $-V_{T,L2w4}$, $-V_{T,w45}$, $-V_{T,w2w5}$, and $-V_{T,\theta 35}$ all increase with time after fault clearance, which causes the oscillation to diverge. From Fig. 6(f)-(h), it can be observed that the magnitudes of interaction energy items $-V_{T,L24}$, $-V_{T,w25}$, and $-V_{T,w4w5}$ all decrease with time, which is conducive to the stable operation of the system. And the magnitudes of $-V_{T,L13}$, $-V_{T,L2w4}$, $-V_{T,\theta 35}$, and $-V_{T,L24}$ are much larger than those of the others. Among them, $-V_{T,\theta 35}$ is the key factor leading to system instability.

When the proposed oscillation suppression strategy is applied 1.5 s after the fault is cleared, the simulation results of DFIG output current and active power and the voltage at PCC are shown in Fig. 7. The results in Fig. 7 prove that the proposed strategy can quickly suppress the diverging oscillation. Besides, the simulation results of the interaction energy in Fig. 2 are shown in Fig. 8, after the application of the proposed strategy.

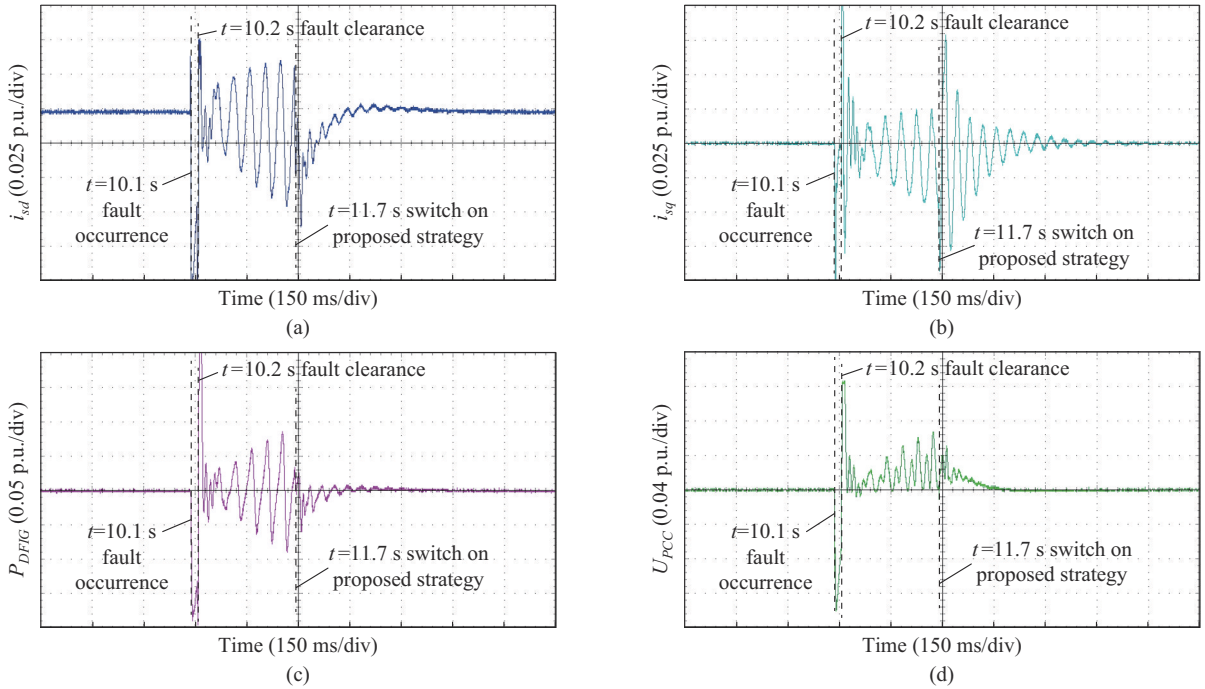

Fig. 7. Simulation results of DFIG output current, output active power, and voltage at PCC when proposed strategy is used. (a) *d*-axis component of DFIG output current. (b) *q*-axis component of DFIG output current. (c) DFIG output active power. (d) Voltage at PCC.

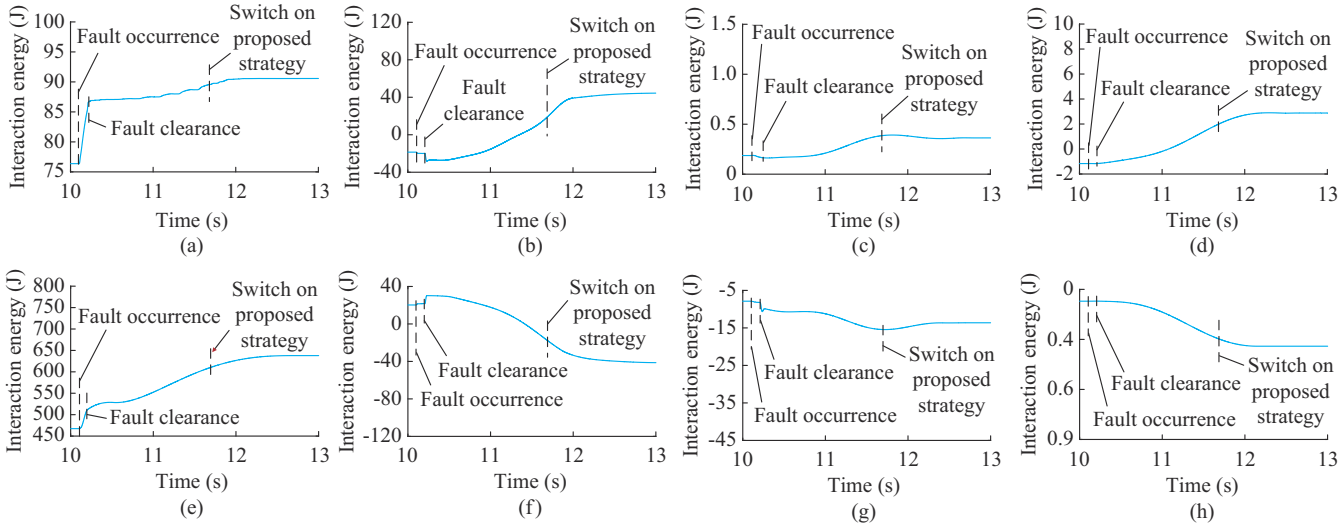

Fig. 8. Change of interaction energy after proposed strategy is used. (a) $-V_{T,L13}$. (b) $-V_{T,L2w4}$. (c) $-V_{T,w45}$. (d) $-V_{T,w2w5}$. (e) $-V_{T,\theta35}$. (f) $-V_{T,L24}$. (g) $-V_{T,w25}$. (h) $-V_{T,w4w5}$.

It can be observed from Fig. 8 that after the proposed oscillation suppression strategy is applied, $-V_{T,L13}$, $-V_{T,L2w4}$, $-V_{T,w45}$, $-V_{T,w2w5}$, and $-V_{T,\theta35}$, which increase with time, rapidly reach the steady-state value. Similarly, $-V_{T,L24}$, $-V_{T,w25}$, and $-V_{T,w4w5}$ also quickly reach the steady-state value. According to Fig. 7, after the application of the proposed strategy, the system returns to stable operation. And before the application of the proposed strategy, the total interaction energy of the system increases with time, finally causing the system instability, as shown in Fig. 9(a). After the proposed strategy is used, the total interaction energy of the system quickly reaches a steady-state value, so the system returns to stable operation, as shown in Fig. 9(b).

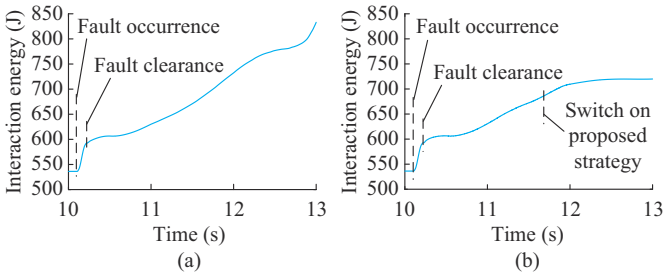

Fig. 9. Simulation results of total interaction energy of system before and after application of proposed strategy. (a) Before application. (b) After application.

Based on the simulation results in Figs. 6-8, the changing trends of the interaction energy links in grid-connected DFIG via VSC-HVDC transmission system conform to the theoretical analysis in Section II. Thus, the theoretical analysis is proven correct.

B. Verification of Performance of Proposed Strategy in Different Fault Scenarios

To verify the performance of the proposed strategy in different fault scenarios, the following simulation scenarios are set up.

1) Scenario 1: a single-phase ground fault occurs at $t=10.1$ s. After 100 ms, the fault is cleared. And the proposed strategy is applied at $t=12.0$ s.

2) Scenario 2: a two-phase ground fault occurs at $t=10.1$ s. After 100 ms, the fault is cleared. And the proposed strategy is applied at $t=12.0$ s.

3) Scenario 3: a two-phase fault occurs at $t=10.1$ s. After 100 ms, the fault is cleared. And the proposed strategy is applied at $t=12.0$ s.

The simulation results of DFIG output current and active power in scenarios 1-3 are shown in Figs. 10-12, respectively. From Figs. 10-12, the system oscillation in different scenarios can be suppressed quickly and smoothly by using the proposed oscillation suppression strategy in this paper. Therefore, it can be applied in different scenarios.

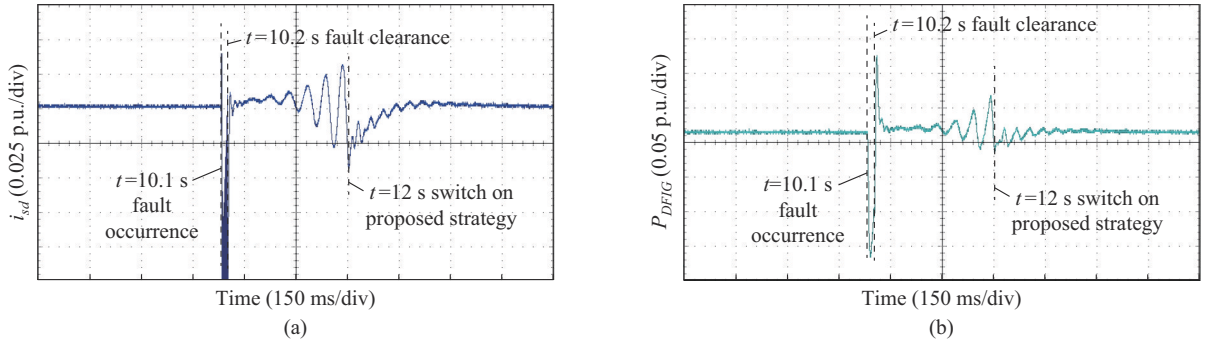

Fig. 10. Simulation results of DFIG output current and active power in scenario 1. (a) *d*-axis component of DFIG output current. (b) DFIG output active power.

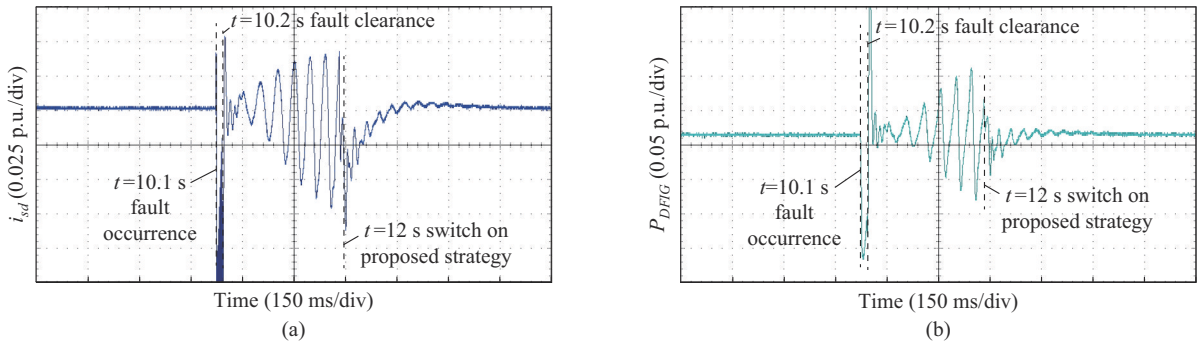

Fig. 11. Simulation results of DFIG output current and active power in scenario 2. (a) *d*-axis component of DFIG output current. (b) DFIG output active power.

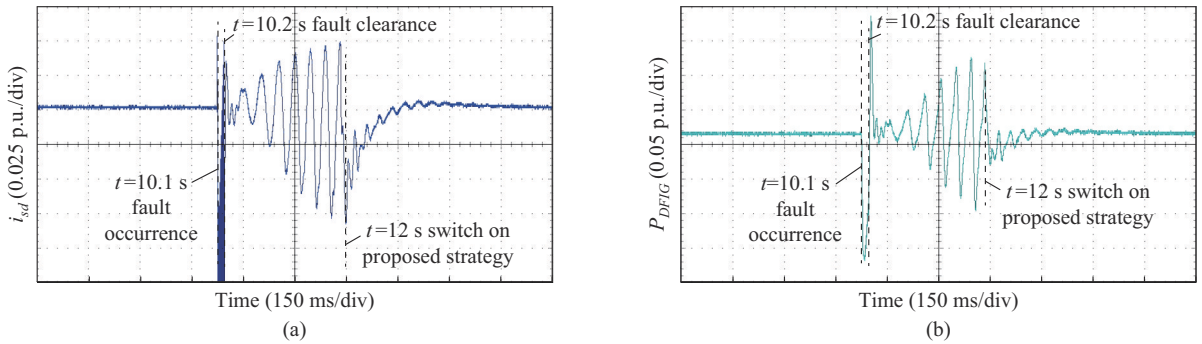

Fig. 12. Simulation results of DFIG output current and active power in scenario 3. (a) *d*-axis component of DFIG output current. (b) DFIG output active power.

C. Effectiveness Comparison with Existing Strategy

The oscillation suppression effectiveness of the proposed strategy has been compared with that of the stability enhancement strategy based on parameter optimization in [28].

In the comparison test, a three-phase grounding fault is set to occur at $t = 10.1$ s, and the fault lasts for 100 ms. The simulation results of DFIG output current and output active power are shown in Fig. 13. The system control parameters adjust to those given in Table II at $t = 11.7$ s.

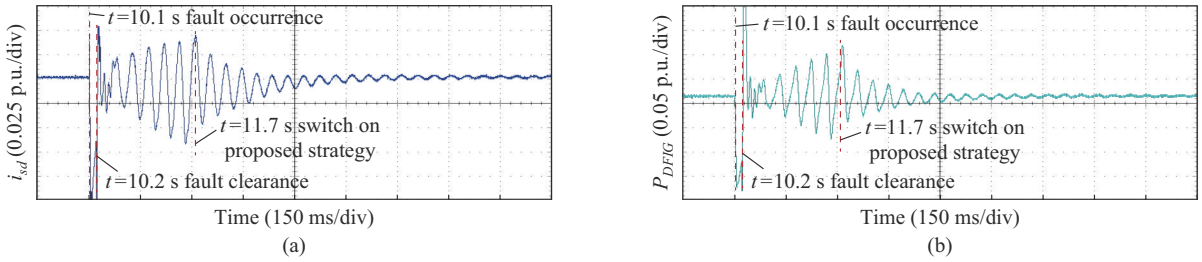

Fig. 13. Simulation results of DFIG output current and active power. (a) *d*-axis component of DFIG output current. (b) DFIG output active power.

It can be observed from Fig. 7(a), Fig. 7(c), and Fig. 13 that compared with the oscillation suppression strategy based on parameter optimization, the proposed strategy in this paper can suppress system oscillation rapidly and smoothly.

V. Conclusion

An oscillation stability analysis suitable for the grid-connected DFIG-based wind farms via VSC-HVDC transmission system is conducted, and an oscillation suppression strategy is proposed for the system after fault clearance. Based on the mathematical models of DFIG and VSC-HVDC, the dynamic energy model of the interconnected system is constructed. By analyzing the influence of each interaction energy item on the system stability, the mechanism of oscillation instability is revealed, and an oscillation suppression strategy is put forward. The main conclusions are as follows.

1) In grid-connected DFIG-based wind farms via VSC-HVDC transmission system, the energy flows will be redistributed when a fault occurs and after the fault is cleared. After fault clearance, the *d*-axis subsystem of GSC current inner loop, PLL, and *q*-axis subsystem of VSC-HVDC voltage outer loop are the key factors that induce the oscillation.

2) The phase compensation branches can effectively reduce the interaction energy between PLL and the subsystem of *d*-axis RSC current inner loop, which is conducive to the system stability. The supplementary damping control branch can increase the dissipation energy of RSC current inner loop subsystems, thus effectively suppressing the transmission of the oscillation energy.

3) The proposed strategy can quickly suppress diverging oscillations in the grid-connected DFIG-based wind farms via VSC-HVDC transmission system. It can help ensure the stable operation without affecting the control performance of the system in normal operation states.

TABLE II
MAIN PARAMETERS AFTER OPTIMIZATION

Item	Parameter	Value
PLL	Proportional coefficient	1.44
	Integral coefficient	37.8
RSC	Outer loop proportional coefficient	3
	Outer loop integral coefficient	5
	Inner loop proportional coefficient	0.33
	Inner loop integral coefficient	7.8
GSC	Outer loop proportional coefficient	8
	Outer loop integral coefficient	400
	Inner loop proportional coefficient	4
	Inner loop integral coefficient	50
Flexible DC converter station	Outer loop proportional coefficient	1
	Outer loop integral coefficient	25
	Inner loop proportional coefficient	1
	Inner loop integral coefficient	6

REFERENCES

[1] Z. Li, R. Zhan, Y. Li *et al*., "Recent developments in HVDC transmission systems to support renewable energy integration," *Global Energy Interconnection*, vol. 1, no. 5, pp. 595-607, Dec. 2018.

[2] Y. Han, H. Sun, B. Huang *et al*., "Discrete-time state-space construction method for SSO analysis of renewable power generation integrated AC/DC hybrid system," *IEEE Transactions on Power Systems*, vol. 37, no. 3, pp. 2322-2334, May 2022.

[3] L. P. Kunjumuhammed, B. C. Pal, R. Gupta *et al*., "Stability analysis of a PMSG-based large offshore wind farm connected to a VSC-HVDC," *IEEE Transactions on Energy Conversion*, vol. 32, no. 3, pp. 1166-1176, Sept. 2017.

[4] J. Sun, "Impedance-based stability criterion for grid-connected inverters," *IEEE Transactions on Power Electronics*, vol. 26, no. 11, pp. 3075-3078, Nov. 2011.

[5] B. Wen, D. Dong, D. Boroyevich *et al*., "Impedance-based analysis of grid synchronization stability for three-phase paralleled converters," *IEEE Transactions on Power Electronics*, vol. 31, no. 1, pp. 26-38, Jan. 2016.

[6] Q. Hu, L. Fu, F. Ma *et al*., "Large signal synchronizing instability of PLL-based VSC connected to weak AC grid," *IEEE Transactions on Power Systems*, vol. 34, no. 4, pp. 3220-3229, Jul. 2019.

[7] X. Li, Z. Tian, X. Zha *et al*., "Nonlinear modeling and stability analysis of grid-tied paralleled-converters systems based on the proposed dual-iterative equal area criterion," *IEEE Transactions on Power Electronics*, vol. 38, no. 6, pp. 7746-7759, Jun. 2023.

[8] X. Li, Z. Tian, X. Zha *et al*., "An iterative equal area criterion for transient stability analysis of grid-tied converter systems with varying damping," *IEEE Transactions on Power Systems*, vol. 39, no. 1, pp. 1771-1784, Jan. 2024.

[9] P. Hu, Z. Xie, Z. Li *et al*., "Impact of phase-locked loop on transient stability by phase portrait analysis method," in *proceedings of 2022 IEEE 17th Conference on Industrial Electronics and Applications (ICIEA)*, Chengdu, China, Dec. 2022, pp. 463-467.

[10] H. Wu and X Wang, "Design-oriented transient stability analysis of PLL-synchronized voltage-source converters," *IEEE Transactions on Power Electronics*, vol. 35, no. 4, pp. 3573-3589, Apr. 2020.

[11] X. Xiong, C. Wu, and F. Blaabjerg, "Effects of virtual resistance on transient stability of virtual synchronous generators under grid voltage sag," *IEEE Transactions on Industrial Electronics*, vol. 69, no. 5, pp. 4754-4764, May 2022.

[12] Y. Tang and Y. Li, "Common Lyapunov function based stability analysis of VSC with limits of phase locked loop," *IEEE Transactions on Power Systems*, vol. 38, no. 2, pp. 1759-1762, Mar. 2023.

[13] M. Z. Mansour, S. P. Me, S. Hadavi *et al*., "Nonlinear transient stability analysis of phased-locked loop-based grid-following voltage-source converters using Lyapunov's direct method," *IEEE Journal of Emerging and Selected Topics in Power Electronics*, vol. 10, no. 3, pp. 2699-2709, Jun. 2022.

[14] A. A. Basheer, K. Palanimuthu, S. R. Lee *et al*., "Efficiency enhancement using fault-tolerant sliding mode control for the PMVG-based WTS under actuator faults," *IEEE Transactions on Industrial Electronics*, vol. 71, no. 1, pp. 513-523, Jan. 2024.

[15] P. G. Drazin, *Nonlinear Systems*. Cambridge: Cambridge University Press, 1992.

[16] Y. Tang, Z. Tian, X. Zha *et al*., "An improved equal area criterion for transient stability analysis of converter-based microgrid considering nonlinear damping effect," *IEEE Transactions on Power Electronics*, vol. 37, no. 9, pp. 11272-11284, Sept. 2022.

[17] Y. Shen, J. Ma, and L. Wang, "Study on DFIG dissipation energy model and low-frequency oscillation mechanism considering the effect of PLL," *IEEE Transactions on Power Electronics*, vol. 35, no. 4, pp. 3348-3364, Apr. 2020.

[18] J. Ma and Y. Shen, "Stability assessment of DFIG subsynchronous oscillation based on energy dissipation intensity analysis," *IEEE Transactions on Power Electronics*, vol. 35, no. 8, pp. 8074-8087, Aug. 2020.

[19] L. Wang, Z. Yang, X. Lu *et al*., "Stability analysis of a hybrid multi-infeed HVDC system connected between two offshore wind farms and two power grids," *IEEE Transactions on Industry Applications*, vol. 53, no. 3, pp. 1824-1833, May-Jun. 2017.

[20] J. Lyu, X. Cai, and M. Molinas, "Optimal design of controller parameters for improving the stability of MMC-HVDC for wind farm integration," *IEEE Journal of Emerging and Selected Topics in Power Electronics*, vol. 6, no. 1, pp. 40-53, Mar. 2018.

[21] A. Moharana, R. Varma, and R. Seethapathy, "SSR alleviation by statcom in induction-generator-based wind farm connected to series compensated line," *IEEE Transactions on Sustainable Energy*, vol. 5, no. 3, pp. 947-957, Jul. 2014.

[22] R. Preece and J. V. Milanovic, "Tuning of a damping controller for multiterminal VSC-HVDC grids using the probabilistic collocation method," *IEEE Transactions on Power Delivery*, vol. 29, no. 1, pp. 318-326, Feb. 2014.

[23] U. Karaagac, S. O. Faried, J. Mahseredjian *et al*., "Coordinated control of wind energy conversion systems for mitigating sub-synchronous interaction in DFIG-based wind farms," *IEEE Transactions on Smart Grid*, vol. 4, no. 5, pp. 2440-2449, Sept. 2014.

[24] A. Chen, D. Xie, D. Zhang *et al*., "PI parameter tuning of converters for sub-synchronous interactions existing in grid-connected DFIG wind turbines," *IEEE Transactions on Power Electronics*, vol. 34, no. 7, pp. 6345-6355, Jul. 2019.

[25] J. Ma, Z. Yang, Y. Zhou *et al*., "Study on the oscillation transmission paths in direct-drive wind farm transmitted via flexible DC system based on dynamic energy flow," *IET Renewable Power Generation*, vol. 16, no. 5, pp. 966-987, Apr. 2022.

[26] D. Xie, J. Feng, C. Lou *et al*., "Small-signal modelling and modal analysis of DFIG-based wind turbine based on three-mass shaft model," *Proceedings of the CSEE*, vol. 33, no. S1, pp. 21-29, Dec. 2013.

[27] J. Ma, Z. Yang, and W. Du, "An active damping control method for direct-drive wind farm with flexible DC transmission system based on the remodeling of dynamic energy branches," *International Journal of Electrical Power & Energy Systems*, vol. 141, p. 108001, Oct. 2022.

[28] Y. Xu, J. Ma, H. Nian *et al*., "Frequency coupling characteristic modeling of DFIG system based on type-1 frequency-locked loop," in *Proceedings of 2018 IEEE Energy Conversion Congress and Exposition (ECCE)*, Portland, USA, Sept. 2018, pp. 942-949.

Jing Ma received the B.S. and Ph.D. degrees from North China Electric Power University, Beijing, China, in 2003 and 2008, respectively. He has been a Visiting Research Scholar with the Bradley Department of Electrical and Computer Engineering, Virginia Polytechnic Institute and State University, Blacksburg, USA, from 2008 to 2009. He is currently a Professor with the School of Electrical and Electronic Engineering, North China Electric Power University. His research interests include power system stability and control.

Ningsai Su received the B.S. degree from Hebei University of Technology, Tianjin, Chian, in 2016, and the M.S. degree from North China Electric Power University, Beijing, Chian, in 2021. He is currently a Ph.D. student with the School of Electrical and Electronic Engineering, North China Electric Power University. His research interests include power system stability and control.

Yawen Deng received the B.S. degree from North China Electric Power University, Beijing, China, in 2021. She is currently a Ph.D. student with the School of Electrical and Electronic Engineering, North China Electric

Power University. Her research interests include modeling and control of grid-tied converters, and stability of power system based on power electronics.

Weifeng Xia is currently an undergraduate in Shenyang Institute of Engineering, Shenyang, Chian. His research interest includes automatic control.

Honglu Xu received the B.S. and M.S. degrees from North China Electric Power University, Beijing, China, in 2017 and 2020, respectively. She is currently a Ph.D. student with the School of Electrical and Electronic Engineering, North China Electric Power University. Her research interests include power system stability and control.

Yaqi Shen received the Ph.D. degree from North China Electric Power University, Beijing, China, in 2022. She is currently a Postdoctor with the School of Electrical and Electronic Engineering, North China Electric Power University. Her research interests include power system stability analysis and control.